Title: Oligodendrocyte progenitor cell responses to inflammatory demyelination with aging in mouse model of multiple sclerosis

Authors: Emily E. Fresenko[1], Camilla N. Bahri[1], Benjamin J. Burson[1], Noor F. Ahmed[1], Davin Packer[1], Benjamin J. Tabor Jr[1], Bogdan Beirowski[1], Wenjing Sun[2], Michelle A. Wedemeyer[3,4], Cole A. Harrington[1*]

Author affiliations and footnotes

[1]The Ohio State University Wexner Medical Center, Department of Neurology, The Neuroscience Research Institute, College of Medicine, Columbus, OH, USA

[2]The Ohio State University Wexner Medical Center, Department of Neuroscience, College of Medicine, Columbus, OH, USA

[3]The Ohio State University Wexner Medical Center, Department of Neurosurgery and Pediatrics, College of Medicine, Columbus, OH, USA

[4]Nationwide Children's Hospital, Division of Neurosurgery, Columbus, OH, USA

Contact information

*Corresponding author:

Cole A. Harrington

460 W 12th Ave, Biomedical Research Tower 604

Columbus, OH 43210

1-614-688-1184

cole.harrington@osumc.edu

Conflict of Interest Statement

The authors have declared that no conflict of interest exists.

Abstract

Oligodendrocyte progenitor cells (OPCs) have the capacity to self-renew, differentiate, and remyelinate the CNS. Aging is associated with a reduction in the functional capacity of OPCs even in the absence of an autoimmune insult. To determine how aging affects the response of oligodendroglia to a strong inflammatory insult comparable to an immune-mediated demyelinating event in multiple sclerosis (MS), we performed adoptive transfer of young myelin-reactive Th17 T cells into young and aged OPC lineage tracing mice. After adoptive transfer, OPCs were enriched within spinal cord lesions of both young and aged mice. However differentiated oligodendrocytes (OLs) were significantly reduced after adoptive transfer. Both young and aged OPCs differentiated into mature OLs during adoptive transfer. Transmission electron microscopy revealed thinly myelinated axons without degenerative features that likely represent remyelinated axons in lesions of both age groups. Young and aged OPCs rise to the challenge after a strong auto-immune attack, suggesting that compensatory strategies permit both young and aged oligodendroglia to survive despite an inflammatory environment. Identifying pathways that promote resilience of oligodendroglia in the face of an inflammatory challenge will facilitate the development of remyelinating therapies for people with MS.

Introduction

In the postnatal CNS, oligodendrocyte progenitor cells (OPCs) are lineage restricted progenitors with the capacity to proliferate, migrate, and differentiate into mature myelinating oligodendrocytes during development and adulthood (1-3) and in response to demyelinating injury (4,5). Multiple sclerosis (MS) is a chronic demyelinating disorder of the CNS in which an autoimmune attack of oligodendroglia and their myelin processes results in demyelinating lesions (6-8). OPCs and maturing oligodendrocytes have been identified in MS lesions from patients of all ages (9,10) suggesting that OPCs may retain the capacity to differentiate and remyelinate after a demyelinating attack despite an inhibitory inflammatory environment (8,11).

53 Aging is a risk factor for progressive accumulation of neurological disability in MS
54 (12,13). Cellular aging in MS leads to senescence of immune cells and other CNS resident cell
55 populations (13) which may influence the ability of aged OPC to differentiate and remyelinate.
56 Physiological aging of OPCs, in the absence of an immune disorder or model, is associated with
57 phenotypic changes in OPC ion channel expression (14), reduced proliferation and
58 differentiation (14,15), increased cellular senescence and upregulation of immune response
59 pathways (14-16). Developmental inhibitors of OPC differentiation, e.g. Wnt and hypoxia
60 inducible factor-1 alpha (HIF-1a) pathways, are upregulated in aged OPCs and pharmacological
61 inhibition of these pathways promotes differentiation of aged OPCs *in vitro* (16). In toxin-
62 mediated demyelination models, OPC proliferation, recruitment into lesions, differentiation and
63 remyelination are all slower in aged animals (17-19). Metformin plus alternative day fasting (15)
64 and young macrophages (20) can partially rescue the slower remyelination kinetics in aged
65 animals. These studies suggest that aged OPC function can be augmented to levels similar to
66 young OPCs, and targeting mechanisms that promote aged OPC function may be a viable
67 therapeutic strategy to promote remyelination in MS.
68 Formal investigations of the impact of aging on OPC performance after an autoimmune-
69 mediated inflammatory insult have not been conducted to date. While toxin-mediated models
70 benefit from stereotyped OPC responses, the lack of an adaptive immune response in these
71 models may not accurately reflect the microenvironment of human MS lesions. Inflammatory
72 models offer the benefit of a T cell mediated auto-immune process targeting oligodendroglia and
73 myelin, better simulating an acute MS demyelinating event (6, 21). Although inflammatory
74 models reproduce the histological features of severe disease, including early axonal
75 degeneration, high inflammatory infiltrate, rapid severe disease course and lack of disease
76 remission (22-24), the rapid progression and severity of clinical disease prevent the use of this
77 model for chronic timepoints. Despite these limitations, the study of murine models with a strong
78 autoimmune inflammatory response may uncover mechanisms that oligodendroglia utilize to

79 adapt to a harsh inflammatory environment. Studies in both murine models (25-31) and human
80 MS tissue (29,32) indicate the oligodendroglia adopt distinct transcriptional states in response to
81 inflammation. These “disease-associated” oligodendroglia upregulate immune signaling
82 pathways and may directly interact with T cells by expression of MHC class I and II molecules
83 (30, 33-34). The function of disease-associated oligodendroglia is unclear and may be context
84 and model dependent. Investigation of OPC properties in a strong inflammatory model will offer
85 insight into how young and aged OPCs respond to an auto-immune demyelinating insult.
86 We performed lineage tracing of OPCs in the Th17 adoptive transfer model to
87 investigate how aging affects the response of OPCs to a robust autoimmune demyelinating
88 event. A tamoxifen-inducible OPC Cre line (*Pdgfra-Cre*^{ERT}) (35) was crossed to an inducible
89 GFP reporter line (*RCE- Rosa26*^{flstopflEGFP}) (36), tamoxifen was administered to lineage trace
90 OPCs starting two weeks prior to adoptive transfer of young myelin-reactive Th17 T cells into
91 aged (10-14 months) and young (3-5 months) *Pdgfra-Cre*^{ERT};*RCE* recipients. The Th17 adoptive
92 transfer model offers several advantages over other immune-mediated models including 1)
93 control of adoptive transfer T cell age to prevent potential confounding from aged donor T cells
94 (37) and 2) selective determination of oligodendroglial responses to a Th17 T cell mediated
95 disease as Th17 T cells play a key role in MS pathogenesis (22, 38-39).
96 Following myelin-reactive Th17 adoptive transfer into *Pdgfra-Cre*^{ERT}*;RCE* mice, we found
97 that OPCs from both young and aged mice were enriched in spinal cord lesions. Higher OPC
98 densities were seen in lesions compared to non-lesion white matter suggesting that the lesion
99 environment promotes OPC recruitment and/or survival mechanisms. Differentiated
100 oligodendrocytes (OLs) were reduced in adoptive transfer in both young and aged animals. A
101 small minority of lineage traced OPCs differentiated into mature OLs in both ages. Transmission
102 electron microscopy (TEM) analysis of lesions identified similar proportions of thinly myelinated
103 axons without degenerative features in both young and aged lesions suggesting that
104 remyelination can occur even in the presence of an ongoing inflammatory response. These

105 findings indicate that both young and aged OPCs respond similarly to an auto-immune
106 inflammatory demyelinating insult and OPCs may have compensatory strategies to support
107 survival and physiological function in an inflammatory environment.
108
109 **Results**
110 *Aged Th17 adoptive transfer animals have increased disease severity*
111 To identify differences in the response of young and aged OPCs to an adaptive auto-
112 immune response, young and aged mice cohorts were used for this study (Figure 1A, age at
113 sacrifice/tissue analysis- young: P87-P148, 3-5 months; aged: P295-P427,10-14 months). Aged
114 mice age range was selected based on mouse aging functional studies correlating our aged
115 animal cohort to human age in 4th decade (40) which is the average onset of late-onset
116 relapsing remitting MS (LORRMS) and progressive MS (41,42). Experiments with aged animals
117 beyond 14 months was not performed due to increased disease severity and early morbidity in
118 our aged cohort (Figure 1B-C). OPC lineage tracing was initiated by administering tamoxifen to
119 young and aged *Pdgfra-Cre*^{ERT}; *RCE* (*Rosa26*^{flstopflEGFP}) mice two weeks prior to adoptive
120 transfer (Figure 1A) to avoid tamoxifen-mediated impairment of T-cell activation and disease
121 induction (43). Myelin oligodendrocyte glycoprotein (MOG)-reactive T cells were generated by
122 immunizing young (2-3-month-old) female wild-type C57BL/6J donors with MOG_{35-55} peptide
123 followed by *ex-vivo* polarization into Th17 phenotype and adoptive transfer into young and aged
124 *Pdgfra-Cre*^{ERT}; *RCE* OPC lineage traced mice. Young and aged *Pdgfra-Cre*^{ERT}; *RCE* mice that
125 were administered tamoxifen but did not receive adoptive transfer served as naïve controls. For
126 transmission electron microscopy analysis (TEM), two additional experimental lines were used:
127 wild-type C57BL/6J mice that did not receive tamoxifen and OPC Cre combined with the
128 *Tau*^{mGFP} reporter (*Pdgfra-Cre*^{ERT}; *Tau*^{mGFP}) which have been previously used to visualize newly
129 formed myelin sheaths (43-45). *Pdgfra-Cre*^{ERT}; *RCE* OPC lineage traced mice were sacrificed at
130 9-10 days post-adoptive transfer, corresponding to peak disease (Figure 1B) for

131 immunohistochemistry analysis of spinal cord. Wild-type and *Pdgfra-Cre*^{ERT}; *Tau*^{mGFP} OPC
132 remyelination reporter mice were sacrificed at 10 days post-adoptive transfer for TEM.
133 Extension of the analysis timepoint in aged mice beyond the acute peak disease time-point was
134 not possible without significant loss of aged animals as one third of aged mice reached humane
135 end-point criteria at day 9 (Figure 1C, score ≥4, no movement around cage, inability to feed).
136 Aged adoptive transfer mice had significantly higher experimental autoimmune
137 encephalomyelitis (EAE) clinical scores relative to young adoptive transfer mice (Figure 1B) and
138 faster onset to quadriplegia (Figure 1C). Increased disease severity in aged Th17 adoptive
139 transfer recipients in other studies is not ameliorated by young bone marrow transplantation
140 indicating that the aged host CNS environment drives an exacerbated disease course (46).
141
142 *Pdgfra-Cre lines lineage trace hematopoietic cells in CNS inflammatory models*
143 Lineage traced *Pdgfra-Cre*^{ERT}*;RCE* mice demonstrated high recombination efficiency
144 and GFP reporter induction in OPCs (Figure 1D) with ~70% of Pdgfra-positive cells expressing
145 GFP (Figure 1E). Lineage traced GFP reporter-positive cells demonstrated expression of pan-
146 oligodendroglial marker Olig2 (Figure 1F). However, this OPC Cre *Pdgfra-Cre*^{ERT} line
147 consistently demonstrated non-oligodendroglial lineage traced cells (GFP+/Olig2-) in adoptive
148 transfer spinal cord particularly within lesions (Figure 1G-H). GFP reporter positive cells were
149 positive for hematopoietic cell marker CD45 and Pdgfra (Figure 1I). Flow cytometry confirmed
150 the presence of a GFP+CD45+ cell population in adoptive transfer CNS tissue (Figure 1J),
151 indicating that peripheral immune cells that traffic into the CNS undergo recombination. These
152 findings highlight the need for rigorous validation of Cre drivers with a lineage tracing approach
153 when using CNS inflammatory disease models. Given the presence of GFP reporter positive
154 non-oligodendroglial cells in adoptive transfer, subsequent quantitative analysis of lineage
155 traced OPCs required inclusion of oligodendroglial restricted markers.
156

157 *Young and aged lineage traced OPCs are enriched within adoptive transfer lesions*

158 In the Th17 adoptive transfer model, immune infiltrates are concentrated at
159 leptomeningeal and perivascular spaces of the spinal cord and hindbrain (47-48). To
160 characterize the impact of aging on OPC density and differentiation in response to T cell
161 adoptive transfer, transverse spinal cord cross-sections from young and aged adoptive transfer
162 and naïve animals were stained for lineage traced OPCs with GFP and pan-oligodendroglial
163 marker Olig2 (Figure 2A). Lineage traced OPCs were quantified in total spinal cord cross-
164 sections, lesions (determined by DAPI hypercellularity), and non-lesional white matter. For initial
165 quantification all lesions present in one spinal cord cross-section were grouped together for the
166 total lesional density (Figure 2B). To capture the differences across lesions within a single spinal
167 cord section, individual lesions were quantified separately for downstream analyses (Figure 2C-
168 F, H). Aged lineage traced OPC (GFP+Olig2+) density was significantly lower in adoptive
169 transfer whole cord compared to young, however aged OPCs were present at similar densities
170 in adoptive transfer compared to aged naïve whole cord (Figure 2B) reflecting lower baseline
171 OPC densities with aging. Lineage traced OPC (GFP+Olig2+) density was not significantly
172 different between aged and young lesions when pooling all lesions across a spinal cord section
173 and not accounting for differentiation status (Figure 2B).

174 To better characterize the fate and differentiation status of lineage traced OPCs, spinal
175 cord sections were co-labeled with GFP, mature oligodendrocyte marker (Aspa), and
176 hematopoietic marker (CD45) followed by quantification of all GFP+CD45- cells in spinal cord
177 cross-sections (Figure 2C-H). In both young and aged animals, lineage traced OPCs that
178 remained OPCs (OPC->OPC, GFP+Aspa-CD45-) were significantly increased within lesions
179 compared to non-lesional white matter (Figure 2C). OPC->OPC density was significantly lower
180 in aged compared to young lesions (Figure 2C). To determine the enrichment of OPCs within
181 lesions compared to surrounding non-lesional white matter, a ratio of mean lesional density over
182 non-lesional white matter (nlwm) density was calculated for each spinal cord cross-section

183 (Figure 2D). Lineage traced OPCs that remained OPCs (GFP+Aspa-CD45-) had a greater than
184 2-fold enrichment in both young and aged lesions compared to surrounding nlwm suggesting
185 recruitment, proliferation, and/or retention of OPCs within the lesional environment.
186
187 *Young and aged OPCs demonstrate the ability to differentiate in acute adoptive transfer*
188 The density of OPCs increased in lesions of young and aged animals, suggesting that
189 despite the more severe disease observed in aged animals, OPCs retain the capacity to
190 respond to demyelination and potentially differentiate. A small minority of lineage traced OPCs
191 underwent differentiation and expressed Aspa (GFP+Aspa+CD45-) in both young and aged
192 adoptive transfer spinal cord (Figure 2E). Compared to non-lesion white matter, differentiated
193 OPCs were significantly higher in young lesions and significantly lower in aged lesions (Figure
194 2E). Young OPCs may have a higher or faster capacity for differentiation within lesions and/or
195 aged OPCs undergoing differentiation may be more susceptible to cell death in the aged
196 environment. Comparing the ratio of newly differentiated OPCs to surrounding nlwm on an
197 individual spinal cord section level (Figure 2F) did not indicate a significant difference between
198 the ratio of differentiated OLs within young and aged lesions compared to surrounding nlwm
199 (Figure 2F). To determine the percentage of lineage traced OPCs that remained OPCs within
200 lesions, all lineage traced OPCs (GFP+CD45-) were quantified within individual lesions and
201 assessed for Aspa expression. Similar to density analysis, lineage traced OPCs that remained
202 OPCs made up over 95% of lineage traced OPCs within lesions of young and aged animals
203 (Figure 2H). The enrichment of lineage traced OPCs within young and aged lesions and ability
204 of OPCs to differentiate, particularly within young lesions at this peak disease time-point,
205 indicates that OPCs can quickly respond even with ongoing inflammatory activity and high
206 disease severity. Alternative immune-mediated models with remission of clinical disease may
207 offer additional insight into the kinetics of OPC responses after resolution of inflammatory
208 activity.

209

210 *Young and aged differentiated oligodendrocytes are lost in adoptive transfer*

211 Adoptive transfer of myelin oligodendrocyte glycoprotein (MOG)-reactive Th17 T cells
212 may result in targeted cytotoxicity to MOG-expressing mature OLs. To determine whether OLs
213 are lost or preserved in young and aged adoptive transfer, spinal cord sections were stained for
214 OL marker Aspa (Figure 3A). High densities of differentiated OLs in spinal cord cross-sections
215 necessitated the development of a semi-automated cell counting method. An ImageJ macro
216 was developed to quantify Aspa-positive cell densities (Figure 3B). Aspa+ OL densities were
217 significantly lower at baseline in aged compared to young naïve spinal cord (Figure 3C).
218 Adoptive transfer resulted in a significant decrease in OL density by ~1/4 of density relative to
219 naïve controls (Figure 3C) and aged adoptive transfer spinal cord had the highest degree of OL
220 loss. To determine if existing OLs (not derived from OPCs) were selectively lost within lesions
221 we performed manual quantification of OLs in individual lesions and adjacent nlwm with use of
222 GFP/Aspa/CD45 co-labeling (Figure 2G). Existing differentiated OLs (Aspa+GFP-CD45-) were
223 significantly lower in lesions compared to non-lesions in both young and aged animals with the
224 lowest density of OLs within aged lesions (Figure 3D). The ratio of OL lesional to non-lesional
225 density was not significantly different between young and aged adoptive transfer (Figure 3E).

226 The lower density of aged OLs throughout spinal cord regions may reflect overall higher
227 disease severity in aged animals and/or increased susceptibility of aged OLs to cell death. To
228 investigate the impact of EAE score and CD45 infiltrate on OPC and OL densities within the
229 spinal cord of young and aged adoptive transfer animals we performed a correlation analysis on
230 matched cell counts from individual spinal cord sections. Variables of age, EAE score,
231 percentage of cord occupied by CD45 infiltrate, and density of OPCs (GFP+Aspa-CD45-), OPC-
232 >OL (GFP+Aspa+CD45-), and OLs (GFP-Aspa+CD45-) across the whole cord and mean of
233 pooled lesions were compared for each spinal cord section (Supplemental Figure 1A). Strong
234 correlations (r values <-0.5 or $>+0.5$ and p values of ≤ 0.001) included the following correlations:

235 positive correlations- age to EAE score, OPCs in cord to OPCs in lesion, OPCs in cord to OPC-
236 >OL in cord, and negative correlation- age to OL lesion. EAE score was not significantly
237 correlated with OPC/OL densities. Degree of CD45 infiltrate was not correlated with age, EAE
238 score or OPC/OL densities. While pooling counts from lesions may limit the power of this
239 analysis, it suggests that the range of EAE scores across aged and young animals does not
240 markedly impact OPC/OL densities. Notably, higher levels of OPCs throughout the whole cord
241 was correlated with higher OPCs within lesions and OPCs that differentiated in the cord. Higher
242 age may also correlate with reduced OL lesional densities which was also suggested by our
243 macro and individual lesional quantification (Figure 3C-D).
244
245 *Aging increases myelin debris accumulation after adoptive transfer*
246 To determine the impact of aging on the degree of axonal loss, myelin debris and
247 demyelination after adoptive transfer, transverse spinal cord sections from young and aged
248 adoptive transfer mice were stained for neurofilament (NF), degraded myelin basic protein
249 (dMBP), and FluoroMyelin (total myelin) (Figure 4). To quantify axonal loss within lesions an
250 ImageJ macro was developed to quantify neurofilament-positive axonal density (Figure 4A).
251 Axonal density was highly variable across lesions, and no significant differences were observed
252 between young and aged lesions (Figure 4B). The accumulation of myelin debris was assessed
253 by the presence of dMBP staining (Figure 4C) and lesions in aged animals had a significantly
254 higher percentage of white matter with positive dMBP staining (Figure 4D). Higher levels of
255 myelin debris in aged animals may reflect impaired myelin debris clearance by aged
256 macrophages (20). Although myelin debris was higher in aged animals, there was no significant
257 differences in percent of white matter demyelination quantified by FluoroMyelin staining
258 between age groups (Figure 4E-F).
259
260 *Remyelination is present to a similar extent in young and aged lesions*

261 In the Th17 adoptive transfer model, areas of demyelination are localized in the
262 peripheral white matter adjacent to leptomeningeal infiltrates indicated by DAPI hypercellularity
263 (Figure 4E) (47-48). To determine if OPCs can remyelinate in adoptive transfer, we crossed
264 OPC inducible Cre line *Pdgfra-Cre*^{ERT} to inducible membrane targeted GFP within the
265 microtubule associated protein tau locus (*Tau*^{mGFP}) which has been used to visualize newly
266 generated myelin sheaths (43-45). Newly generated OL GFP+ myelin sheaths were not seen in
267 naïve spinal cord (Figure 5A). In adoptive transfer, GFP+ processes surrounding axons and co-
268 labeled with MBP were visualized at the edge of lesions (Figure 5B) suggesting the presence of
269 remyelination from newly formed OLs. Immunohistochemistry of a young and aged adoptive
270 transfer cohort of remyelination reporter mice (*Pdgfra-Cre*^{ERT}*;Tau*^{mGFP}) was performed however
271 quantification of remyelination was not pursued due to GFP reporter background expression in
272 OPC processes in the parenchyma (Figure 5B).
273 To more reliably assess remyelination transmission electron microscopy (TEM) was
274 performed on wild-type C57BL/6J young and aged ventromedial white matter lesions at 10 days
275 post-adoptive transfer. Longer time-point analysis was not possible in aged animals due to
276 increased morbidity in this model (Figure 1C). Ventromedial white matter was chosen based on
277 the high rate of lesions in this region, ability to identify landmarks with the presence of a ventral
278 vein, and large diameter axons (49) that could facilitate the ability to detect thinner remyelinated
279 axons. Toxin-mediated demyelinating models have demonstrated that remyelinated axons can
280 be identified by thinner myelin sheaths (50-52), however thin myelin sheaths can also be a sign
281 of degenerating axons both in toxin-mediated and immune-mediated models (53). Perivascular
282 immune infiltrates lining areas of demyelination were identified in all ventromedial white matter
283 sections imaged as well as high concentration of oligodendrocytes within demyelinated areas
284 (Figure 5C). Thin myelin sheaths surrounding axons with degenerative features (electron dense
285 material, myelin blebbing, myelin infoldings, myelin unraveling, high mitochondrial
286 concentration) and axons without these degenerative features were present within lesions

287 (Figure 5D). TEM lesion images at 1150x magnification were used for quantification of young
288 and aged lesions with inverted images facilitating the visualization of myelin sheaths and axonal
289 components (Figure 5E). G-ratio quantification was performed on 1150x magnification images
290 of young and aged ventromedial white matter lesions (non-inverted) using MyelTracer (54)
291 combined with manual outlining for axons with a diameter ≥2μm. Axons with thin myelin sheaths
292 were noted to have g-ratios of 0.8 or higher. Axons with g-ratio ≥ 0.8 were present in both age
293 groups. G-ratio slopes were significantly different between young and aged lesions (Figure 5F).
294 Relative frequency distribution analysis of g-ratios demonstrated a significantly higher frequency
295 of lower g-ratios (thicker myelin) in aged lesions (Figure 5G), indicating that the difference in g-
296 ratio slope was driven by thicker myelin sheaths in aged compared to young animals. This
297 finding is consistent with previous studies of human (55) and mouse spinal cord tracts (56)
298 which have demonstrated thicker myelin with aging. With thin myelin sheaths surrounding both
299 degenerating axons and axons without degenerative components (Figure 5D) we further
300 analyzed axons with thin myelin sheaths (g-ratio ≥0.8) for the presence or absence of
301 degenerative features. Thinly myelinated axons without degenerative features, likely
302 representing remyelinated axons, were present in similar proportions in aged and young
303 adoptive transfer lesions (Figure 5H). Thinly myelinated axons with degenerative features were
304 also present at similar proportions in young and aged lesions (Figure 5I). Relative frequency
305 distribution analysis of axonal cross-sectional area of thinly myelinated axons classified as
306 degenerating compared to non-degenerating indicated that degenerating axons had a
307 significantly higher frequency of large axonal areas (Figure 5J) as would be expected for
308 degenerating axons.
309 We acknowledge that thin myelin sheaths may represent remyelinated axons or axons in
310 the process of demyelination and our time-point analysis at 10 days-post adoptive transfer
311 would require fast kinetics for OPC differentiation and remyelination. Young and aged OPC

312 remyelination reporter mice *Pdgfra-Cre*^{ERT}*;Tau*^{mGFP} that received adoptive transfer were
313 processed for TEM with immunogold staining for GFP to attempt to further validate OPC
314 remyelination. However, due to GFP reporter expression in OPC processes in the parenchyma
315 (Figure 5B) and anti-GFP immunogold deposition in similar pattern, analysis of
316 TEM/immunogold was not further pursued. Despite these limitations, remyelination appears
317 similar between age groups, even in the presence of a robust inflammatory infiltrate and severe
318 disease model.
319
320 **Discussion**
321 OPCs are dynamic cells with the ability to self-renew, migrate, and differentiate into
322 mature, myelinating oligodendrocytes. Although the response of OPCs to demyelination has
323 been investigated in toxin-mediated models and genetic ablation strategies (5), the fate of OPCs
324 after exposure to a robust auto-immune inflammatory insult remains poorly understood.
325 Biological aging influences multiple sclerosis disease activity and progression (13) and the
326 response of OPCs in an aged environment is particularly relevant for a chronic CNS
327 autoimmune disease that affects individuals at all stages of life. Physiological aging in the
328 absence of a disease model is associated with a decreased rate of OPC proliferation (14,16)
329 and differentiation into mature OLs (14). Aged OPCs express higher levels of the cell cycle
330 inhibitors p16 and p21, which may reflect age-associated senescence (57). In response to toxin-
331 mediated demyelination insults, aged OPCs have slower proliferation, recruitment, and
332 differentiation kinetics; however, remyelination in aged animals eventually catches up to young
333 animals (17-19).
334 To determine whether aging impacts the response of OPCs to a strong adaptive immune
335 response akin to an acute MS attack, we performed lineage tracing of OPCs in young adult and
336 aged spinal cord after adoptive transfer of myelin reactive Th17 polarized T cells. Both aged and
337 young OPCs respond to an acute inflammatory demyelination event with a proportionally similar

338 increase in lesional OPC density. The highest densities of lineage traced OPCs in both aged
339 and young animals were within lesions, suggesting that compensatory mechanisms allow for
340 recruitment, survival and persistence of OPCs within a lesion environment. Both young and
341 aged OPCs can differentiate into mature OLs, a response that is less robust in aged OPCs.
342 While existing differentiated OLs sustain damage after adoptive transfer, the magnitude of aged
343 OL loss is more severe. Although the presence of ongoing axonal degeneration in adoptive
344 transfer and other models can complicate the interpretation of thin myelin sheaths by TEM
345 analysis (53), we quantified thin myelin sheaths by TEM and found a similar proportion of non-
346 degenerative and likely remyelinated axons in lesions of young and aged animals. With TEM we
347 were unable to distinguish whether remyelination occurs from newly generated
348 oligodendrocytes versus existing differentiated oligodendrocytes, both of which can occur in
349 toxin-mediated models (4). Further lineage tracing studies using other transgenic membrane
350 targeted reporter lines may offer additional insight into the origin of remyelinating
351 oligodendroglia in immune-mediated models.
352 Previous studies combining genetic CNS interferon gamma production with toxin-
353 mediated demyelination indicate that OPCs may by targets of CD8 T cell mediated killing (33).
354 Our findings in the Th17 adoptive transfer model indicate that an inflammatory lesion
355 environment stimulates OPCs responses and both young and aged OPCs may have
356 compensatory strategies that allow them to survive and differentiate despite the presence of T
357 cells. Interferon-response pathways are upregulated in disease-associated oligodendroglia (25-
358 32) and with physiological aging (16, 58) which may be a result of CD8 T cell accumulation
359 within the aged CNS (58). Oligodendrocytes upregulate MHC class I (59) and immune
360 checkpoint inhibitor programmed death-ligand 1 (PD-L1) (60) in CNS viral models. Upregulation
361 of interferon-response pathway in young and aged OPCs may in fact be beneficial for
362 oligodendroglial survival allowing OPCs and OLs to evade the immune attack and dampen
363 immune signaling. Further studies are needed to investigate the role of disease-associated

364 oligodendroglia in inflammatory models to determine whether immunoregulatory pathways in
365 oligodendroglia are beneficial or inhibitory to oligodendroglial function.
366 This study demonstrates that oligodendroglia in young and aged animals respond
367 similarly to an acute auto-immune mediated demyelinating attack mediated by MOG-reactive
368 Th17 T cells. The ability of both young and aged OPCs to respond to a severe autoimmune
369 attack and preservation of OPCs within lesions suggests that remyelination and repair strategies
370 that target oligodendroglial survival mechanisms may be promising strategy for people of all
371 ages with MS.
372
373 **Methods**
374 Sex as a biological variable
375 Both male and female mice transgenic and wild-type mice were used as adoptive transfer
376 recipients with a roughly equal even distribution between female and male mice in young and
377 aged cohorts. Due to the research strategy involving use of transgenic lines, timing of adoptive
378 transfer cohorts and need for aged cohorts, all available positive transgenic mice were used
379 regardless of sex and the experiments were not sufficiently powered to assess differences
380 between sexes. Wild-type mice used for immunization for donor T cells were female only to
381 avoid potential sex-based T cell differences.
382
383 Animal care and use
384 Young (P87-P148, 3-5-month-old) and aged (P295-P427,10-14-month-old) *Pdgfra-Cre*^{ERT}
385 hemizygote +/- (Jackson Laboratory 018280); *RCE- Rosa26*^{flstopflEGFP} hemizygote +/- (Jackson
386 Laboratory 032037-JAX, MMRRC stock #32027). Young (P131, 4-month-old) and aged (P366-
387 P426, 12-14-month-old) C57BL/6J (Jackson Laboratory 000664) wild-type mice and *Pdgfra-*
388 *Cre*^{ERT} hemizygote +/- (Jackson Laboratory 018280); *Tau*^{mGFP} hemizygote +/- (Jackson
389 Laboratory 021162) were used for transmission electron microscopy experiments. Age indicated

390 is animal age at sacrifice. Female and male mice were assigned to experiments based on
391 availability. Mice were maintained on a 12-hour light/dark cycle, housed in cages of five or less,
392 and provided food and water ad libitum. Adoptive transfer mice were monitored daily between
393 days 4-10 post-adoptive transfer for clinical score and weight. All animal experiments were
394 conducted in accordance with the National Institute of Health Guide for the Care and Use of
395 Laboratory Animals.
396
397 Adoptive transfer/Experimental autoimmune encephalomyelitis (EAE)
398 Transgenic mice *Pdgfra-Cre*^{ERT}; *RCE* and *Pdgfra-Cre*^{ERT}*;Tau*^{mGFP} were administered tamoxifen
399 (Sigma T5648) intraperitoneally (100-150ul of 10mg/ml stock reconstituted in corn oil for
400 working dose of 75mg/kg/day) daily for 5 days to induce recombination starting two weeks prior
401 to adoptive transfer. Wild-type C57BL/6J mice used for transmission electron microscopy (TEM)
402 did not receive tamoxifen. T cells for adoptive transfer were generated from wild-type C57BL/6J
403 (Jackson Laboratory 000664) 2-3-month-old female mice which were anesthetized with
404 intraperitoneal injection of ketamine (90mg/kg)/ xylazine (10mg/kg) and immunized with four
405 subcutaneous flank injections with a total of 0.2-0.4mg of myelin oligodendrocyte glycoprotein
406 $(MOG)_{35-55}$ peptide (1mg/ml, biosynthesis) resuspended in Complete Freund's Adjuvant (CFA)
407 with concentration of 5mg/ml heat killed *M. tuberculosis*. After 10 days immunized wild-type
408 mice were euthanized with CO_2 and spleen and lymph nodes were dissected and placed on ice
409 in EAE media: RPMI (ThermoFisher 21870084), 10% FBS (GeminiBio 100-106-500), P/S
410 (Fisher 15-140-148), 1x GlutaMAX (Fisher 35-050-061), 1x NEAA (ThermoFisher 11140050),
411 1mM sodium pyruvate (Fisher 11-360-070), 55nM beta-mercaptoethanol (ThermoFisher
412 21985023). Spleens and lymph nodes were mashed across filter, washed with EAE media, and
413 centrifuged at 800g 5min. Spleens were resuspended in RBC lysis buffer (ThermoFisher 00-
414 4300-54) for 2 minutes at room temperature followed by quenching with EAE media, centrifuged
415 at 800g 5min, and washed with EAE media. Spleen and lymph nodes were resuspended in EAE

416 media with MOG_{35-55} peptide (50μg/ml, Biosynthesis), recombinant mouse IL-23 (8ng/ml, R&D
417 1887-ML), recombinant mouse IL-1a (10ng/ml, ThermoFisher 211-11A), anti-IFNg (10mg/ml,
418 Bio X Cell BE0055) at volume of $5x10^6$ cells/ml in T75 flasks. Cells suspensions were incubated
419 at 37°C in 5% CO_2 incubator for 3.5 days. After *ex-vivo* Th17 polarization cells were collected
420 into conical tubes, centrifuged 800g 5min, filtered and washed twice with MACs buffer (0.5%
421 BSA and 2mM EDTA in PBS). CD4 T cell selection was performed with mouse CD4 (L3T4)
422 microbeads (Miltenyi Biotec 130-117-043) with LS column per Miltenyi protocol. Eluted CD4+
423 cells were washed in MACs buffer twice and $4x10^6$ cells were injected intraperitoneally into
424 transgenic mice (tamoxifen administered) and wild-type mice (no tamoxifen). For naïve/non-
425 adoptive transfer animals, littermates of transgenic mice that received tamoxifen were separated
426 into naïve cages. Mice were monitored daily starting on day 4 post-adoptive transfer with
427 weights and EAE clinical scoring scale. EAE scoring scale: 0.5 reduced tail tone; 1 complete
428 loss of tail tone; 1.5 slight gait imbalance; 2 gait imbalance with footfalls or spinning/ataxia; 2.5
429 hindlimb foot drag able to move above hip; 3 partial to complete hindlimb paralysis, not able to
430 move either hindlimb above hip, moving around cage with forelimbs; 3.5 complete hindlimb
431 paralysis, hindlimbs held to one size, moving around cage with forelimbs; 4 complete hindlimb
432 paralysis, hindlimbs held to one size, no movement around cage but alert; 4.5 moribund not
433 alert; 5 death. Mice were sacrificed at days 9-10 post-adoptive transfer with most severe mice
434 sacrificed on day 9 time-point to avoid death and following end-point euthanasia protocols
435 (euthanasia at score 4 or greater within 24 hours or sustained weight loss ≥30% for 3 days). All
436 mice in this study were between clinical scores of 2-4.5 at day of sacrifice and a total of 5
437 separate cohorts of adoptive transfer were performed. EAE clinical score graphs from mice
438 used for immunohistochemistry and transmission electron microscopy including several
439 additional cohorts that were used to optimize TEM fixation protocol were combined for EAE
440 clinical score graphs. There was no significant difference between mice that received tamoxifen

441 and those that did not. Animals that were sacrificed due to endpoint criteria or reached score 5
442 (death) were included as data-points with score 5 on subsequent days on EAE clinical scoring
443 graphs.
444
445 Immunohistochemistry
446 Mice were anesthetized with intraperitoneal injection of ketamine (90mg/kg)/ xylazine (10mg/kg)
447 and perfused transcardially with 15ml of 0.1M phosphate-buffered saline (PBS) followed by cold
448 4% paraformaldehyde (PFA) in PBS (ThermoScientific J19943.K2). Spinal cords were dissected
449 out of the spinal column and post-fixed in 4% PFA/PBS at 4°C overnight then cryoprotected in
450 30% sucrose/1xPBS at 4°C for at least 2 days. Prior to embedding two transverse cuts were
451 performed (at the end of the cervical enlargement and beginning of lumbar enlargement) to
452 separate the spinal cord into cervical, thoracic and lumbar segments. Spinal cord segments
453 were embedded in Tissue-Tek OCT compound (Sakura) with a cross-section of the beginning of
454 each spinal cord segment facing the cutting edge of the block. Spinal cord blocks were
455 sectioned at 15μm thickness with Leica CM1950 cryostat onto Superfrost Plus microscope
456 slides (Fisher 12-550-15) with each 8-10 series of slides having four sets of
457 cervical/thoracic/lumbar transverse sections (12 total sections) representing ~600mm distance
458 from first to fourth section in each region to obtain representative analysis across each spinal
459 cord segment on one slide. Slides were stored at -80°C until use. For immunostaining slides
460 were permeabilized with 1xPBS +0.1% Triton-X100 (PBST) for 10 minutes followed by outlining
461 of sections with PAP pen (ThermoFisher 008899). To prevent non-specific binding, 5% normal
462 goat serum (JacksonImmuno 005-000-121) in PBST was added to sections for 1 hour at room
463 temperature followed by addition of primary antibodies in same blocking solution overnight at
464 4°C. Slides were washed in PBST three times 5 minutes each followed by incubation in
465 secondary antibodies in blocking buffer for 1 hour at room temperature. Slides were washed
466 with PBST twice for 5 minutes each, once with PBS for 5 minutes then mounted with

467 ProlongGold antifade (ThermoFisher P36935). For FluoroMyelin co-stained slides, FluoroMyelin
468 Red (Invitrogen F34652) was added at 1:300 dilution in PBS after last wash and incubated for
469 20 minutes followed by PBS wash and mounting. The following primary antibodies were used:
470 chicken anti-GFP (Abcam ab13970, 1:1000), rabbit anti-Olig2 (MilliporeSigma ab9610, 1:1000),
471 rabbit anti-Aspa (MilliporeSigma ABN1698, 1:250), rat anti-CD45 (MilliporeSigma 05-1416,
472 1:500), rabbit anti-degraded myelin basic protein dMBP (MilliporeSigma ab5864, 1:1000), rabbit
473 anti-Pdgfra (CellSignaling 3174, 1:500), mouse anti-neurofilament heavy NF-H (EnCor MCA-
474 AH1), rat ant-MBP (Biorad MCA409S, 1:1000), mouse anti-neurofilament medium NF-M
475 (Invitrogen 130700, 1:1000, for remyelination reporter staining). The following secondary
476 antibodies were used all purchased from Invitrogen and used at dilution of 1:500: Alexa Fluor
477 488 goat anti-chicken IgY (H+L) (A-11039), Alexa Fluor 594 goat anti-rat IgG (H+L) (A-11007),
478 Alexa Fluor 647 goat anti-rat IgG (H+L) (A-21247), Alexa Fluor 647 goat anti-rabbit IgG (H+L)
479 (A-21245), Alexa Fluor 647 goat anti-mouse IgG (H+L) (A-21236), and Alexa Fluor 594 goat
480 anti-mouse IgG (H+L) (A-11032).
481
482 Immunohistochemistry imaging and analysis
483 Images of immunohistochemistry-stained spinal cord sections were acquired using Olympus
484 IX83 inverted microscope with Zeiss ZEN microscopy software. Tiled images of transverse
485 spinal cord sections at a resolution of 650nm/pixel (10x objective) were obtained for GFP/Olig2,
486 GFP/Aspa, and dMBP stains. Higher resolution tiled images at 325nm/pixel (20x objective) were
487 taken for GFP/Aspa/CD45, neurofilament and FluoroMyelin stains. For manual-counting, image
488 stacks were analyzed in ImageJ/Fiji using channels tool, cell counter and ROI manager. For
489 macro-analyzed images (DAPI/GFP/Aspa and DAPI/GFP/NF stains), images were exported as
490 non-compressed TIFF grayscale stack of channels. Macros were developed using a
491 combination of background subtraction, moments thresholding and analyzing particle
492 ImageJ/Fiji functions to identify positive cells. In refinement of macros for individual stains,

493 quality assessment images with overlay of counted objects were analyzed for accuracy and
494 parameters were adjusted for each macro to obtain the highest accuracy of cell detection. After
495 importing the spinal cord section image stack, the macros prompt the user to outline regions of
496 interest (ROI)- whole cord, gray matter and lesions. Lesions were identified and outlined by the
497 presence of DAPI hypercellularity which correlated with CD45 infiltrate. Non-lesion white matter
498 counts were generated by subtracting whole cord counts from gray matter and total lesion
499 counts, this was due to the ease in outlining gray matter during the macro execution compared
500 to total non-lesion white matter. For Aspa macro counts total lesions within each spinal cord
501 section were outlined as one lesion. In NF macro and DAPI/GFP/Aspa/CD45 manual counts
502 individual lesions were outlined separately to increase power of analysis given potential
503 variability across lesions. For neurofilament quantification, DAPI/GFP/NF 20x tiled images were
504 analyzed with NF macro allowing users to outline lesions based on DAPI hypercellularity and
505 NF positive axonal density was calculated for individual lesions. For dMBP quantification
506 DAPI/GFP/dMBP 10x tiled image stacks were quantified in ImageJ/Fiji by outlining total white
507 matter area and white matter with positive dMBP staining for each spinal cord section. For
508 FluoroMyelin quantification, DAPI/GFP/Fluoromyelin 20x tiled image stacks were quantified by
509 outlining total white matter and demyelinated white matter without Fluoromyelin. To generate
510 non-biased transverse spinal cord cross-section counts throughout the cervical, thoracic and
511 lumbar spinal cord, all spinal cord sections without significant folds or other tissue processing
512 artifacts were imaged. Adoptive transfer sections without lesions were not quantified to focus on
513 spinal cord regions with inflammatory infiltrate. Sections quantified per animal: GFP/Olig2 6-16,
514 GFP/Aspa/CD45 hand counts 3-6, GFP/Aspa macro 6, GFP/NF macro 3-8, GFP/FlouroMyelin
515 6-9, GFP/dMBP 6-12. Sections counts were not averaged across individual animals to focus on
516 comparisons on an individual section/region level which allowed for analysis of enrichment
517 within lesions compared to non-lesion white matter. Lesion to non-lesion cell density ratios were
518 generated by calculating the ratio of average lesional density/average non-lesional density for

519 each spinal cord transverse section. For remyelination reporter assessment *Pdgfra-*
520 *Cre*^{ERT};*Tau*$^{mGFP+/-}$ ventral medial lumbar spinal cord stained with GFP/MBP/NF were imaged on
521 W1 SoRA spinning disk confocal with Nikon NIS-Elements using 40x oil objective (108nm/pixel)
522 with z-stacks and maximum intensity projections generated for ROIs.
523
524 Transmission electron microscopy (TEM)
525 Young (P131, 4-month-old) and aged (P366-P426, 12-14-month-old) C57BL/6J (Jackson
526 Laboratory 000664) wild-type mice and *Pdgfra-Cre*^{ERT} hemizygote +/- (Jackson Laboratory
527 018280); *Tau*^{mGFP} hemizygote +/- (Jackson Laboratory 021162) were used for transmission
528 electron microscopy experiments. C57BL/6J mice were perfused with 4% PFA/5%
529 glutaraldehyde and *Pdgfra-Cre*^{ERT};*Tau*^{mGFP} mice for immunogold were perfused with 4%
530 PFA/0.25% glutaraldehyde. On day 10 post-adoptive transfer young and aged EAE mice were
531 anesthetized with intraperitoneal injection of ketamine (90mg/kg)/ xylazine (10mg/kg) and
532 perfused transcardially with 15ml of 0.1M PBS followed by cold fixation solution: PFA (EMS
533 15714-S) and glutaraldehyde (EMS 16210) in 80mM sodium cacodylate and 9mM calcium
534 chloride dihydrate in EM grade dH_2O (EMS 22800-01) pH 7.4. The spinal cord was dissected
535 out of the column and post-fixed for 24 hours in perfusion buffer (2 hours for immunogold
536 followed by switch to 1% PFA overnight). Spinal cord was cut into 2mm transverse segments on
537 spinal cord matrix (EMS 69085-C) and 3-5 lumbar and 3-5 cervical blocks per animal were
538 washed with wash buffer (70mM sodium cacodylate, 70mM sodium chloride, 0.5mM calcium
539 chloride, 1mM magnesium chloride hexahydrate in EM grade dH_2O) for 30 minutes followed by
540 post-fixation in 1% osmium tetroxide (EMS 19152) in 100mM sodium cacodylate for 1 hour
541 protected from light. Blocks were washed with EM grade dH_2O twice 2 minutes each then
542 transferred to glass vials followed by dehydration (50% EtOH, 70% EtOH, 80% EtOH, 95%
543 EtOH, 100% EtOH x 2, 100% propylene oxide 2 times, with each wash 30 minutes). Blocks
544 were incubated overnight in 1:1 Embed 812 resin (EMS 14120, medium hardness

545 concentration):propylene oxide (EMS 20412) at room temperature. Solution was changed to 3:1
546 Embed 812 resin:propylene oxide for 24 hours followed by 100% Embed 812 resin for 24 hours
547 at room temperature. Embedding molds were filled with fresh Embed 812 resin and individual
548 spinal cord blocks were transferred to molds and baked at 60°C for 24 hours. Semi-thin sections
549 from lumbar spinal cord blocks were cut on Leica Ultracut UCT at 1μm thickness with Histo
550 Diamond Knife (EMS 60-HIS) and stained with 1% toluidine blue to visualize lesions. Ultrathin
551 sections for TEM were cut on Ultra Diamond Knife (EMS 40-UL) at 70nm thickness on
552 Ultramicrotome Reichert Ultracut E and mounted onto grids (Pelco 200 mesh 1GC200). Grids
553 were stained using Hiraoka staining kit (EMS 71560-00) with uranyl acetate alternative (EMS
554 22405) for 20 minutes followed by rinses in EMS grade dH_2O 30 seconds 3 times, then
555 incubation in 3mg/ml lead citrate in 0.1N NaOH in dH_2O for 3 minutes. Grids were washed with
556 20mM NaOH followed by 2 washes with dH_2O for 30 seconds then air dried. For immunogold
557 grids were stained with Hiraoka staining kit washed with 0.01% Triton TBS, blocked with 1%
558 NGS (JacksonImmuno 005-000-121), 1% BSA (Sigma A4161), 1% fish gelatin (Sigma G7041)
559 in TBST (0.01% Triton TBS) for 30 minutes then incubated with anti-GFP (Abcam ab13970,
560 1:100) overnight at 4°C. Grids were washed with TBST 3 times, incubated in 12nm colloidal
561 gold donkey anti-chicken (JacksonImmuno 703-205-155) in blocking solution for 90 minutes at
562 room temperature. Grids were washed with TBST, post-fixed in 1% glutaraldehyde in PBS for 5
563 minutes, washed in EM grade dH_2O followed by staining for myelin as described above. Grids
564 were imaged on FEI Tecnai G2 Spirit TEM and ventral side was identified by the presence of
565 ventral central vein and ventromedial white matter regions were imaged at 1150x magnification.
566 All lumbar blocks were sectioned, imaged and quantified. All lumbar blocks from aged and
567 young animals contained lesions with notable loss of myelin and presence of immune infiltrate in
568 this region. TEM lesion images acquired at 1150x resolution representing one grid box were
569 analyzed in MyelTracer (54) with users selecting and manually outlining myelin sheaths for all
570 axons with ≥2μm given the difficulty in outlining smaller diameter axons at this magnification and

571 desire to quantify remyelination which is more feasible for large diameter axons. Axon diameter
572 and axon plus myelin diameters and calculated g-ratios were exported and compiled in excel
573 and g-ratios were plotted with a cutoff of 2μm axon diameter in GraphPad Prism. For
574 quantification of thin myelin sheaths with or without degenerative axon components TEM lesion
575 images acquired at 1150x resolution were inverted in ImageJ/Fiji for highlighting myelin sheaths
576 and degenerative axon components. Axons with g-ratio of 0.8 or less with a high number of
577 mitochondria, myelin infoldings, unraveling or blebbing, and/or electron dense material were
578 counted as thinly myelinated axons with degenerative features. Axons with g-ratio of 0.8 or less
579 without these features were counted as without degenerative features and likely remyelinated
580 axons. The percentage of these two types of axons was quantified over total myelinated axons
581 with 2μm or greater axon diameter for each 1150x lesion TEM image. Total myelinated axons
582 with 2μm or greater axon diameter were counted by using StarDist ImageJ/Fiji plugin followed
583 by manual confirmation and adjustment as needed.
584
585 Flow cytometry
586 Transgenic *Pdgfra-Cre*^{ERT}; *RCE- Rosa26*^{flstopflEGFP} mice that received tamoxifen and Th17 T cells
587 or no Th17 T cells (naïve) as described above were sacrificed at 9 days post adoptive transfer
588 for flow cytometry analysis of GFP reporter expression. Mice were anesthetized with
589 intraperitoneal injection of ketamine (90mg/kg)/xylazine (10mg/kg) and perfused transcardially
590 with 15ml of 0.1M PBS. Brains and spinal cord were dissected and dissociated in 20U/ml papain
591 and 100U/ml of DNase in papain buffer (1mM EDTA, 5mM L-cystine, EBSS pH 7.4-7.6) for 30-
592 45 minutes in 37°C 5% CO_2 incubator with 3-4 manual trituration steps during incubation to
593 dissociate into single cell suspension. Dissociated cells were spun at 800g 5min 4°C and
594 resuspended in 30% Percoll (VWR 89428-524) in FACs buffer (2% FBS in PBS no cations) and
595 spin 1000g 10 minutes 4°C speed 8. Myelin layer was removed and pellet was resuspended in

596 FACs buffer followed by transfer over 70mm filter, PBS wash and resuspension in PBS with Fc
597 block (BD Biosciences rat anti-mouse CD16/CD32 552142, 1:200) and viability stain
598 (eBioscience 65-0865-14, 1:1000) for 10 minutes on ice. Cells were washed in FACs buffer and
599 resuspended in primary antibody CD45 e450 (Invitrogen 48-0451-82 1:100) in FACs and
600 incubated 30 minutes on ice followed by wash and resuspension in FACs. Flow cytometry of
601 spinal cord and brain samples was performed with BD FACS Melody 4-way sorter and analyzed
602 in FlowJo software.
603
604 Statistics and reproducibility
605 GraphPad Prism was used to generate graphs and perform statistical analysis. EAE scoring and
606 quantification was blinded by use of genotyping animal ID that was later linked to a sample
607 group in GraphPad prism analysis. A target sample size of 6 mice per group for
608 immunohistochemistry and 4 mice per group for TEM were set for our analysis. For IHC
609 analysis, average EAE score at sacrifice for young was 3.5 (minimum 2.5, maximum 4.5) and
610 aged 3.8 (minimum 2.5, maximum 4.5) with male and females in both groups. A minimum of 4
611 animals per group and 3 sections per animal were analyzed for IHC outcomes and individual
612 section and lesion data-points were represented to allow for more robust statistics given
613 potential variability on a micro and macroenvironment level within different lesions and sections.
614 For transmission electron microscopy on wild-type mice a total of 4 young and 6 aged wild-type
615 Th17 AT mice were sacrificed and processed with an average EAE score at sacrifice for young
616 was 2.3 (minimum 2, maximum 2.5) and aged 3.6 (minimum 2.5, maximum 4) with males and
617 females in both groups. All lumbar spinal cord blocks were quantified from these animals. In
618 each figure and legend, the number of biological replicates and regions of interest (ROI)
619 quantified, statistical test and significance levels are indicated. Due to complexity of variability
620 including recombination, EAE severity, region, lesional difference and age; datasets did not
621 meet normality assumptions. Statistical significance was assessed using nonparametric Mann-

Whitney (two-tailed) and 2-sample median bootstrap (100,000 resamples, two-tailed, shift bootstrap, BCa bias-corrected & accelerated), with bootstrap preferred with better control for Type I errors and unequal variances (61).

Study approval

All animal experiments were conducted in accordance with the National Institute of Health Guide for the Care and Use of Laboratory Animals and were approved by The Ohio State University Institutional Animal Care and Use Committee (IACUC) protocol 2023A00000086.

Data availability

Data presented in available in the Supporting Data Values file. All macro codes have been made publicly available in GitHub-https://github.com/coleayden/spinalcordmacros. For additional data inquires contact the corresponding author

Author contributions

CAH conceptualized the project. WS, MAW, and BB provided scientific guidance. EEF and CAH conducted the experiments. EEF, CNB, NFA and BJT performed quantification of histology. BJB, EEF, CNB, and NFA performed quantification of transmission electron microscopy. DP developed initial macro code and CAH modified macro codes. CAH wrote the manuscript. All authors contributed to editing and finalizing the manuscript.

Funding support

This study was funded by The Ohio State University College of Medicine Research Innovator Career Development Award (RICDA) and American Academy of Neurology Career Development Award. BJT was funded by the National Multiple Sclerosis Society Undergraduate Summer Research Program.

Acknowledgements

We would like to thank the following contributors: Dr. Benjamin M. Segal for scientific mentorship and access to shared equipment used for this study. Dr. Dana McTigue and Dr. Anthony Brown for assistance with transmission electron microscopy protocols and equipment usage. For equipment used for TEM sectioning and TEM imaging we acknowledge resources from the Campus Microscopy and Imaging Facility (CMIF) and the OSU Comprehensive Cancer Center (OSUCCC) Microscopy Shared Resource (MSR), The Ohio State University. This facility is supported in part by grant P30 CA016058, National Cancer Institute, Bethesda, MD. We would like to thank Jeffery Tonniges CMIF director for providing personal training for TEM ultrathin sectioning.

References

1. Bergles DE, Richardson WD. Oligodendrocyte Development and Plasticity. *Cold Spring Harb Perspect Biol*. 201;8(2):a020453.
2. Zhang X,et al. Replenishing the Aged Brains: Targeting Oligodendrocytes and Myelination? *Front Aging Neurosci*. 2021;13:760200.
3. Rawji KS, Neumann B, Franklin RJM. Glial aging and its impact on central nervous system myelin regeneration. *Ann N Y Acad Sci*. 2023;1519(1):34–45.
4. Franklin RJM, Frisén J, Lyons DA. Revisiting remyelination: Towards a consensus on the regeneration of CNS myelin. *Semin Cell Dev Biol*. 2021;116:3–9.
5. Tepavčević V, Lubetzki C. Oligodendrocyte progenitor cell recruitment and remyelination in multiple sclerosis: the more, the merrier? *Brain*. 2022;145(12):4178–92.
6. Gold R, Linington C, Lassmann H. Understanding pathogenesis and therapy of multiple sclerosis via animal models: 70 years of merits and culprits in experimental autoimmune encephalomyelitis research. *Brain*. 2006;129(Pt 8):1953–71.

674 7. Lassmann H. Multiple sclerosis: lessons from molecular neuropathology. *Exp Neurol*.
675 2014;262 Pt A:2–7.
676 8. Franklin RJM, Simons M. CNS remyelination and inflammation: From basic mechanisms to
677 therapeutic opportunities. *Neuron*. 2022;110(21):3549–65.
678 9. Chang A, et al. NG2-positive oligodendrocyte progenitor cells in adult human brain and
679 multiple sclerosis lesions. *J Neurosci*. 2000;20(17):6404–12.
680 10. Chang A, et al. Premyelinating oligodendrocytes in chronic lesions of multiple sclerosis. *N*
681 *Engl J Med*. 2002;346(3):165–73.
682 11. Antel JP, et al. Immunology of oligodendrocyte precursor cells in vivo and in vitro. *J*
683 *Neuroimmunol*. 2019;331:28–35.
684 12. Stankoff B, et al. Age at onset determines the occurrence of the progressive phase of
685 multiple sclerosis. *Neurology*. 2007;68(10):779–81.
686 13. Graves JS, et al. Ageing and multiple sclerosis. *Lancet Neurol*. 2023;22(1):66–77.
687 14. Spitzer SO, et al. Oligodendrocyte Progenitor Cells Become Regionally Diverse and
688 Heterogeneous with Age. *Neuron*. 2019;101(3):459–71.e5.
689 15. Neumann B, et al. Metformin Restores CNS Remyelination Capacity by Rejuvenating Aged
690 Stem Cells. *Cell Stem Cell*. 2019;25(4):473–85.e8.
691 16. Heo D, et al. Transcriptional profiles of mouse oligodendrocyte precursor cells across the
692 lifespan. *Nat Aging*. 2025;5(4):675–90.
693 17. Shields SA, et al. Remyelination occurs as extensively but more slowly in old rats compared
694 to young rats following gliotoxin-induced CNS demyelination. *Glia*. 1999;28(1):77–83.
695 18. Sim FJ, et al. The age-related decrease in CNS remyelination efficiency is attributable to an
696 impairment of both oligodendrocyte progenitor recruitment and differentiation. *J Neurosci*.
697 2002;22(7):2451–9.
698 19. Shen S, et al. Age-dependent epigenetic control of differentiation inhibitors is critical for
699 remyelination efficiency. *Nat Neurosci*. 2008;11(9):1024–34.

700 20. Ruckh JM, et al. Rejuvenation of regeneration in the aging central nervous system. *Cell*
701 *Stem Cell*. 2012;10(1):96–103.
702 21. Lassmann H. The changing concepts in the neuropathology of acquired demyelinating
703 central nervous system disorders. *Curr Opin Neurol*. 2019;32(3):313–9.
704 22. Rangachari M, Kuchroo VK. Using EAE to better understand principles of immune function
705 and autoimmune pathology. *J Autoimmun*. 201;45:31–9.
706 23. Kipp M, et al. Multiple sclerosis animal models: a clinical and histopathological perspective.
707 *Brain Pathol*. 2017;27(2):123–37.
708 24. Packer D, Fresenko EE, Harrington EP. Remyelination in animal models of multiple
709 sclerosis: finding the elusive grail of regeneration. *Front Mol Neurosci*. 2023;16:1207007.
710 25. Shen K,et al. Multiple sclerosis risk gene Mertk is required for microglial activation and
711 subsequent remyelination. *Cell Rep*. 2021;34(10):108835.
712 26. Pandey S, et al. Disease-associated oligodendrocyte responses across neurodegenerative
713 diseases. *Cell Rep*. 202;40(8):111189.
714 27. Hou J, et al. Transcriptomic atlas and interaction networks of brain cells in mouse CNS
715 demyelination and remyelination. *Cell Rep*. 2023;42(4):112293.
716 28. Aboelnour EL, et al. A comparative transcriptomic analysis of mouse demyelination models
717 and Multiple Sclerosis lesions. [preprint]. http://dx.doi.org/10.1101/2025.03.24.645058.
718 Posted on bioRxiv. March 25, 2025.
719 29. Kukanja P,et al. Cellular architecture of evolving neuroinflammatory lesions and multiple
720 sclerosis pathology. *Cell.* 2024;187(8)1990-2009.
721 30. Falcão AM, et al. Disease-specific oligodendrocyte lineage cells arise in multiple sclerosis.
722 *Nat Med*. 2018;24(12):1837–44.
723 31. Harrington EP, et al. MHC class I and MHC class II reporter mice enable analysis of immune
724 oligodendroglia in mouse models of multiple sclerosis. *Elife*. 2023;12:eLife82938.

725 32. Jäkel S, et al. Altered human oligodendrocyte heterogeneity in multiple sclerosis. Nature.
726 2019;566(7745):543–7.
727 33. Kirby L, et al. Oligodendrocyte precursor cells present antigen and are cytotoxic targets in
728 inflammatory demyelination. *Nat Commun*. 2019;10(1):3887.
729 34. Harrington EP, Bergles DE, Calabresi PA. Immune cell modulation of oligodendrocyte
730 lineage cells. *Neurosci Lett*. 2020;715:134601.
731 35. Kang SH, et al. NG2+ CNS glial progenitors remain committed to the oligodendrocyte
732 lineage in postnatal life and following neurodegeneration. *Neuron*. 201;68(4):668–81.
733 36. Sousa VH, et al. Characterization of Nkx6-2-derived neocortical interneuron lineages. *Cereb*
734 *Cortex*. 2009;19 Suppl 1(Suppl1):i1–10.
735 37. Doss PMIA, et al. Male sex chromosomal complement exacerbates the pathogenicity of
736 Th17 cells in a chronic model of central nervous system autoimmunity. *Cell Rep*.
737 2021;34(10):108833.
738 38. Fletcher JM, et al. T cells in multiple sclerosis and experimental autoimmune
739 encephalomyelitis. *Clin Exp Immunol*. 2010;162(1):1-11.
740 39. Maddur MS, et al. Th17 cells: biology, pathogenesis of autoimmune and inflammatory
741 diseases, and therapeutic strategies. *Am J Pathol*. 2012;181(1):8-18.
742 40. Yanai S, Endo S. Functional Aging in Male C57BL/6J Mice Across the Life-Span: A
743 Systematic Behavioral Analysis of Motor, Emotional, and Memory Function to Define an
744 Aging Phenotype. *Front Aging Neurosci*. 2021;13:697621.
745 41. Tremlett H, et al. Natural history comparisons of primary and secondary progressive multiple
746 sclerosis reveals differences and similarities. *J Neurol*. 2009;256(3):374-381.
747 42. D'Amico E, et al. Late-onset and young-onset relapsing-remitting multiple sclerosis:
748 evidence from a retrospective long-term follow-up study. *Eur J Neurol*. 2018;25(12):1425-
749 1431.

750 43. Bebo BF Jr, et al. Treatment with selective estrogen receptor modulators regulates myelin
751 specific T-cells and suppresses experimental autoimmune encephalomyelitis. *Glia*.
752 2009;57(7):777-790.
753 43. Mei F, et al. Accelerated remyelination during inflammatory demyelination prevents axonal
754 loss and improves functional recovery. *Elife*. 2016 Sep 27;5:e18246.
755 44. Wang, F, et al. Myelin degeneration and diminished myelin renewal contribute to age-
756 related deficits in memory. *Nature Neurosci*. 2020;23(4):481-486.
757 45. Chen, J, et al. Enhancing myelin renewal reverses cognitive dysfunction in a murine model
758 of Alzheimer's disease. *Neuron*. 2021;109(14):2292-2307.e5
759 46. Atkinson JR, et al. Biological aging of CNS-resident cells alters the clinical course and
760 immunopathology of autoimmune demyelinating disease. JCI Insight. 2022;7(12):e158153.
761 47. Stromnes IM, et al. Differential regulation of central nervous system autoimmunity by T(H)1
762 and T(H)17 cells. *Nat Med*. 2008;14(3):337–42.
763 48. Jäger A, et al. Th1, Th17, and Th9 effector cells induce experimental autoimmune
764 encephalomyelitis with different pathological phenotypes. *J Immunol*. 2009;183(11):7169–77.
765 49. Zaimi A, et al. AxonDeepSeg: automatic axon and myelin segmentation from microscopy
766 data using convolutional neural networks. *Sci Rep*. 2018;8(1):3816.
767 50. Blakemore WF. Demyelination of the superior cerebellar peduncle in the mouse induced by
768 cuprizone. *J Neurol Sci*. 1973;20(1):63–72.
769 51. Blakemore WF. Pattern of remyelination in the CNS. *Nature*. 1974;249(457):577–8.
770 52. Neumann B, et al. Problems and Pitfalls of Identifying Remyelination in Multiple Sclerosis.
771 *Cell Stem Cell*. 2020;26(5):617–9.
772 53. Schäffner E, et al. Myelin insulation as a risk factor for axonal degeneration in autoimmune
773 demyelinating disease. *Nat Neurosci*. 2023;26(7):1218-1228.
774 54. Kaiser T, et al. MyelTracer: A semi-automated software for myelin g-ratio quantification.
775 *eNeuro*. 2021;8(4):ENEURO.0558–20.2021.

776 55. Poulen G, et al. Sex and age differences in glia and myelin in nonhuman primate and
777 human spinal cords: implications for pathology. *Cell Death Discov*. 2025;11(1):129.
778 56. Xie F, et al. Effects of normal aging on myelin sheath ultrastructures in the somatic
779 sensorimotor system of rats. *Mol Med Rep*. 2014;10(1):459–66.
780 57. Zhang P, et al. Senolytic therapy alleviates Aβ-associated oligodendrocyte progenitor cell
781 senescence and cognitive deficits in an Alzheimer's disease model. *Nat Neurosci*.
782 2019;22(5):719–28.
783 58. Kaya T, et al. CD8+ T cells induce interferon-responsive oligodendrocytes and microglia in
784 white matter aging. *Nat Neurosci*. 2022;25(11):1446–57.
785 59. Pan R, et al. Oligodendrocytes that survive acute coronavirus infection induce prolonged
786 inflammatory responses in the CNS. *Proc Natl Acad Sci U S A*. 2020;117(27):15902–10.
787 60. Phares TW, et al. Target-dependent B7-H1 regulation contributes to clearance of central
788 nervous system infection and dampens morbidity. *J Immunol*. 2009;182(9):5430–8.
789 61. Johnston MG, Faulkner C. A bootstrap approach is a superior statistical method for the
790 comparison of non-normal data with differing variances. *New Phytol*. 2021;230(1):23-26.

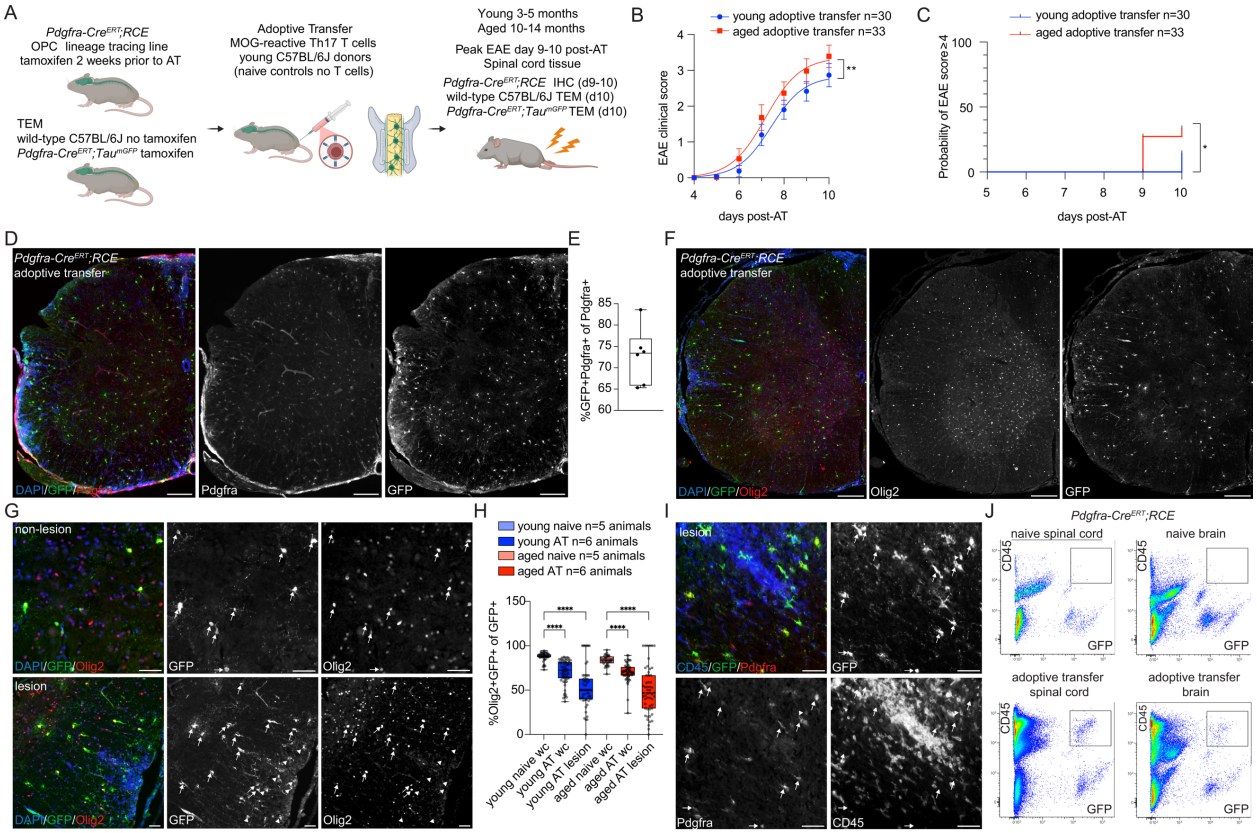

Figure 1- OPC lineage tracing strategy in young and aged Th17 adoptive transfer

(A). Experimental strategy for MOG-reactive Th17 adoptive transfer (AT) in young and aged *Pdgfra-Cre^{ERT};RCE* OPC lineage traced mice (for immunohistochemistry), wild-type C57BL/6J (for TEM), and *Pdgfra-Cre^{ERT};Tau^{mGFP}* OPC remyelination mice (for TEM immunogold). No adoptive transfer young and aged *Pdgfra-Cre^{ERT};RCE* OPC lineage traced mice (for immunohistochemistry) served as naïve controls. Created in BioRender. **(B)**. EAE clinical scoring of all young and aged adoptive transfer animals. Aged adoptive transfer animals have significantly higher EAE clinical scores compared to young animals. All young and aged experimental animals pooled. Two-way repeated measures ANOVA, age ** $p \leq 0.001$. Non-linear regression sigmoidal variable slope lines, error bars 95% CI. (**C**). Kaplan-Meier survival analysis of probability of EAE score of 4 or greater (quadriplegia, euthanasia endpoint) in young and aged adoptive transfer with significant difference in time to score 4 endpoint. Logrank (Mantel-Cox) test, * $p \leq 0.05$. (**D**). Representative images of *Pdgfra-Cre^{ERT};RCE* Th17 adoptive transfer spinal cord with lineage-traced OPCs labeled with GFP antibody and Pdgfra. (**E**). Quantification of OPC recombination efficiency in naïve young and aged *Pdgfra-Cre^{ERT};RCE* by percentage of GFP+Pdgfra+ of total Pdgfra+ cells in whole spinal cord section. Data points mean individual animals, n=6 animals. (**F**). Representative images of *Pdgfra-Cre^{ERT};RCE* Th17 adoptive transfer spinal cord co-labeled with pan-oligodendroglial marker Olig2. (**G**). Lineage traced GFP+ OPCs express Olig2 (arrows) in spinal cord non-lesion and lesion areas. GFP+Olig2- cells (arrowheads) are present particularly within lesions. (**H**). Quantification of the percentage of lineage traced GFP+Olig2+ of total GFP+ cells in whole cord (wc) and lesions. Percentage of GFP+ cells that are oligodendroglia (Olig2+) are significantly lower in adoptive transfer wc and lesions compared to naïve wc in both young and aged animals. Median shift Bootstrap test, ****$p<0.0001$. (**I**). Representative image of lineage-traced *Pdgfra-Cre^{ERT};RCE* adoptive transfer spinal cord lesion co-labeled with GFP, Pdgfra and CD45. GFP+Pdgfra+CD45- OPCs (arrows) and GFP+Pdgfra+CD45+ cells (arrowhead) are present within lesions. (**J**). Flow cytometry of lineage traced *Pdgfra-Cre^{ERT};RCE* naïve and adoptive transfer brain and spinal cord with GFP+CD45+ cells (box) in adoptive transfer tissue. Box and whiskers plots: box 25 to 75 percentile, whiskers min to max, median line, show all datapoints. Scale bars: D,F 200μm; G,I 50μm.

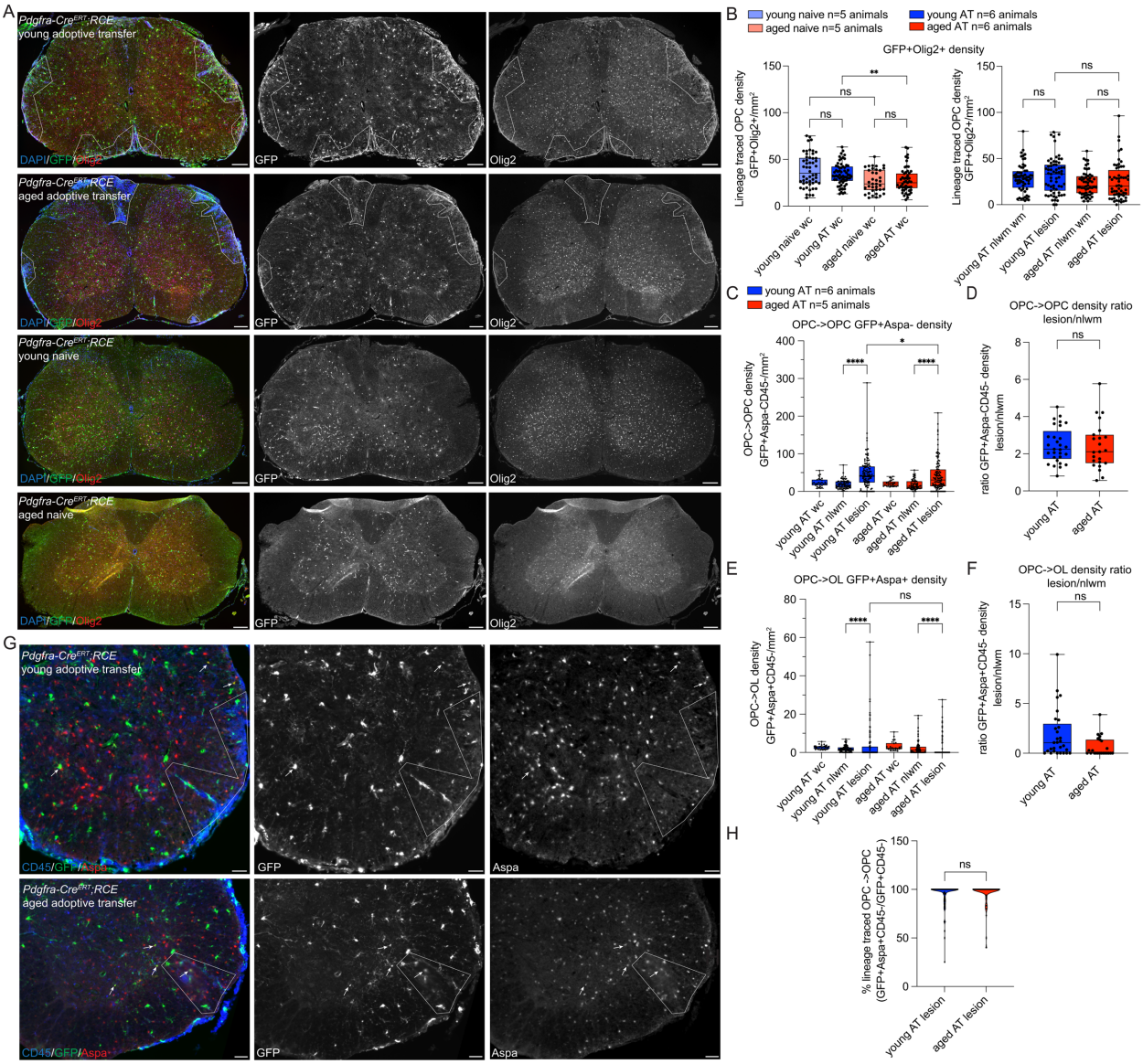

Figure 2- Young and aged lineage traced OPCs are enriched within adoptive transfer lesions
(A). Representative images of young and aged lineage traced OPC (*Pdgfra-Cre^{ERT};RCE*) naïve and adoptive transfer spinal cord cross-sections stained for pan-oligodendroglial marker (Olig2), lineage traced OPCs (GFP) and DAPI (lesions outlined). (**B**). Quantification of lineage traced OPC (Olig2+GFP+) densities in whole cord (wc), adoptive transfer (AT) non-lesion white matter (nlwm) and adoptive transfer lesions. Lesion white matter density datapoints are means of all lesions in an individual spinal cord section. Median shift Bootstrap test. (**C**). Quantification of density of lineage traced OPCs that remained OPCs (OPC->OPC, GFP+Aspa-CD45-) in young and aged adoptive transfer wc, nlwm, and individual lesions. OPC->OPC density is significantly higher in lesions compared to nlwm in young and aged AT. OPC->OPC density is significantly lower in aged compared to young AT lesions. Median shift Bootstrap test. (**D**). Quantification of the ratio of mean OPC->OPC density in lesions compared to nlwm across a whole spinal cord section. OPC->OPC density is enriched in lesions compared to surrounding nlwm in both young and aged AT and lesion/nlwm ratios are not significantly different between ages. Median shift Bootstrap test. (**E**). Quantification of density of lineage traced OPCs that differentiated into OLs (OPC->OL, GFP+Aspa+CD45-) in young and aged adoptive transfer wc, nlwm, and individual lesions. Differentiated OPCs OPC->OL density is significantly higher in lesions compared to nlwm in young and aged AT. Median shift Bootstrap test. (**F**). Quantification of the ratio of mean OPC->OL density in lesions compared to nlwm across a whole spinal cord section. OPC->OL lesion/nlwm ratios are not significantly different between ages. Median shift Bootstrap test. (**G**). Representative images of young and aged *Pdgfra-Cre^{ERT};RCE* adoptive transfer spinal cord stained for GFP, Aspa, and CD45. OPCs that have differentiated (GFP+Aspa+) are indicated with arrows. Lesions outlined by presence of DAPI hypercellularity (not shown) and CD45 infiltrate. (**H**). Quantification of percentage of lineage traced OPCs that remain OPCs (GFP+Aspa-CD45- of GFP+CD45-) within young and aged individual lesions. Median shift Bootstrap test. Box and whiskers plots: box 25 to 75 percentile, whiskers min to max, median line, show all datapoints. p values: ns p>0.05, * p≤0.05, **p≤0.01, ***p≤0.001, ****p<0.0001. Scale bars: A, 200μm; F 50μm.

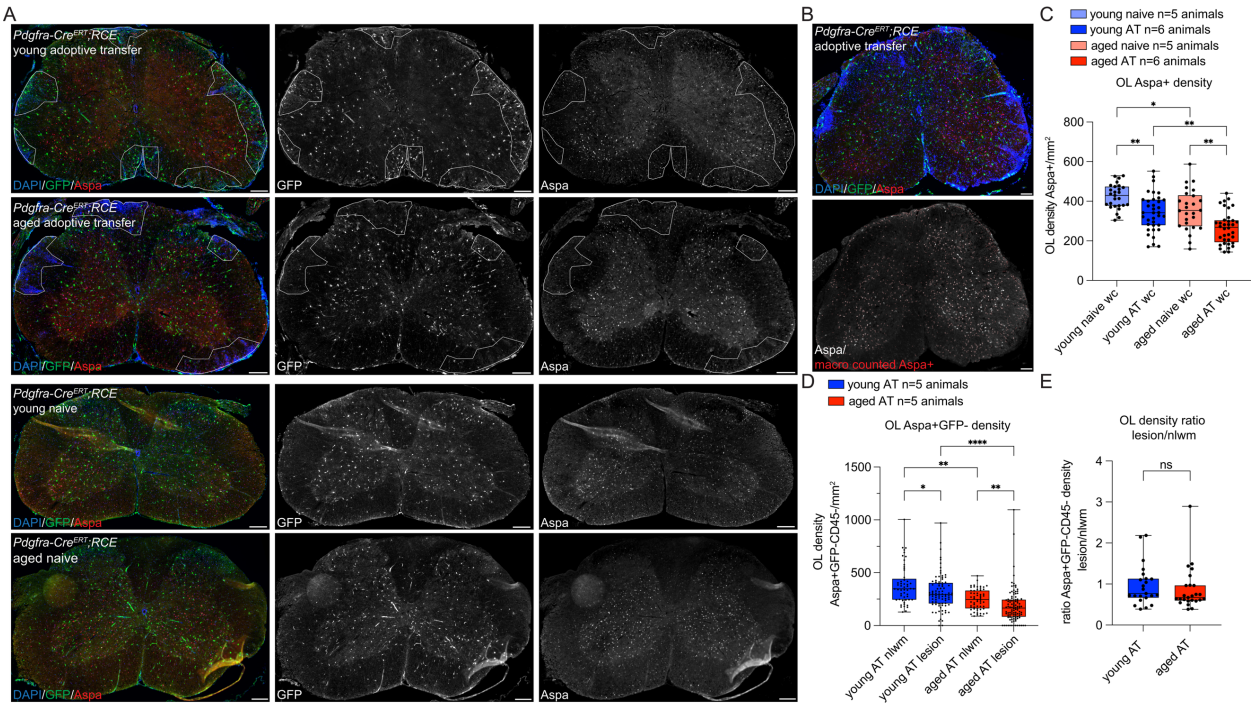

Figure 3- Differentiated oligodendrocytes are reduced in adoptive transfer

(A). Representative images of spinal cord sections from young and aged lineage traced OPC *Pdgfra-Cre^{ERT};RCE* adoptive transfer and naïve spinal cord sections stained for differentiated oligodendrocyte (OL) marker (Aspa), lineage traced OPCs (GFP) and DAPI (lesion areas outlined). (**B**). Representative adoptive transfer spinal cord section stained for DAPI/GFP/Aspa and processed with GFP/Aspa ImageJ macro with Aspa-positive macro counted cells outlined in red overlayed on raw grayscale of Aspa staining (bottom panel). (**C**). Quantification of Aspa+ OL densities with macro in young and aged naïve and adoptive transfer (AT) whole cord (wc) cross-sections. Aspa+ OL density is significantly lower in aged naïve compared to young naïve and in adoptive transfer compared to naïve in both ages. Median shift Bootstrap test. (**D**). Manual quantification of differentiated OLs (GFP-Aspa+CD45-) in young and aged adoptive transfer non-lesion white matter (nlwm) and individual lesions. OL density is significantly lower in lesions compared to nlwm in both ages. Aged AT OL density is significantly lower than young AT in both regions. Median shift Bootstrap test. (**E**). Quantification of the ratio of mean OL density in lesions compared to nlwm across a whole spinal cord section. OL lesion/nlwm ratios are not significantly different between ages. Median shift Bootstrap test. Box and whiskers plots: box 25 to 75 percentile, whiskers min to max, median line, show all datapoints. p values: ns $p>0.05$, * $p\leq0.05$, ** $p\leq0.01$, **** $p<0.0001$. Scale bars: A,B 200μm.

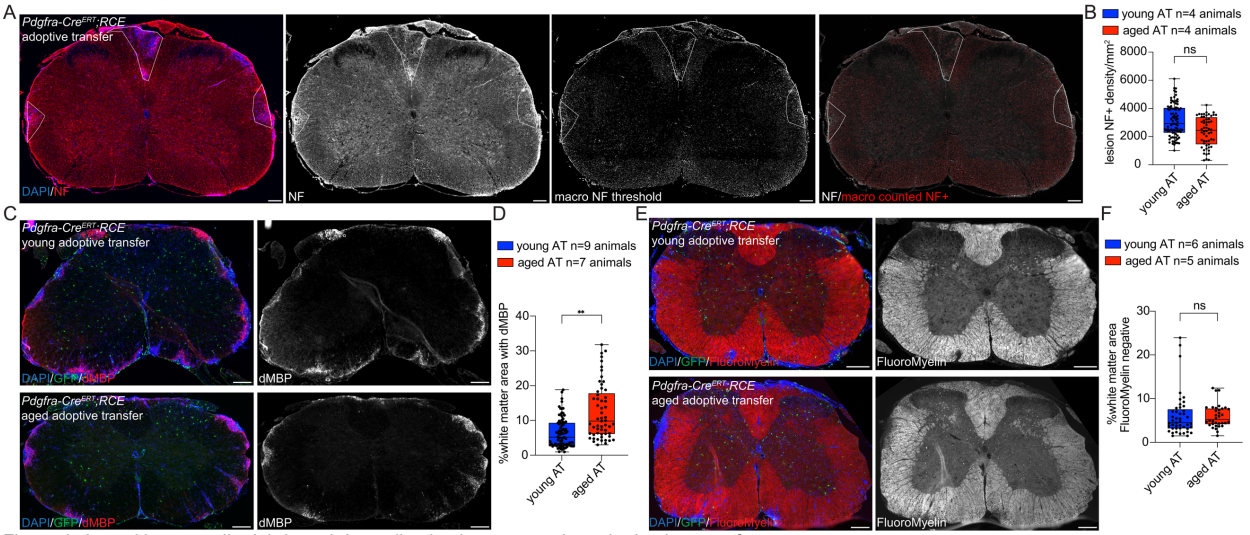

Figure 4- Axonal loss, myelin debris and demyelination in young and aged adoptive transfer

(A). Representative images of macro quantification of axonal density in *Pdgfra-Cre^{ERT};RCE* adoptive transfer spinal cord section stained for neurofilament-H (NF) and DAPI (left panel), NF only grayscale image (middle left panel), NF macro thresholded image (middle right panel) and NF macro processed image with NF+ axons outlined in red (right panel). Lesions outlined. (**B**). Quantification of NF axonal density by macro in individual lesions of young and aged adoptive transfer (AT). No significant difference in axonal density in lesions between ages. Median shift Bootstrap test. **(C)**. Representative image of myelin debris/degraded myelin (dMBP) and GFP staining in young and aged *Pdgfra-Cre^{ERT};RCE* adoptive transfer spinal cord sections. (**D**). Quantification of the percentage of white matter area with dMBP staining in young and aged AT spinal cord with significant increase white matter with myelin debris in aged white matter. Median shift Bootstrap test. (**E**). Representative images of FluoroMyelin and GFP staining in young and aged adoptive transfer *Pdgfra-Cre^{ERT};RCE* spinal cord sections. White matter regions with DAPI hypercellularity demonstrate absence of FluoroMyelin staining. (**F**). Quantification of the percentage of demyelinated white matter with no FluoroMyelin staining in young and aged AT spinal cord with no significant difference between ages. Median shift Bootstrap test. Box and whiskers plots: box 25 to 75 percentile, whiskers min to max, median line, show all datapoints. p values: ns $p>0.05$, $^{**}p\leq0.01$. Scale bars: A,C,E 200μm.

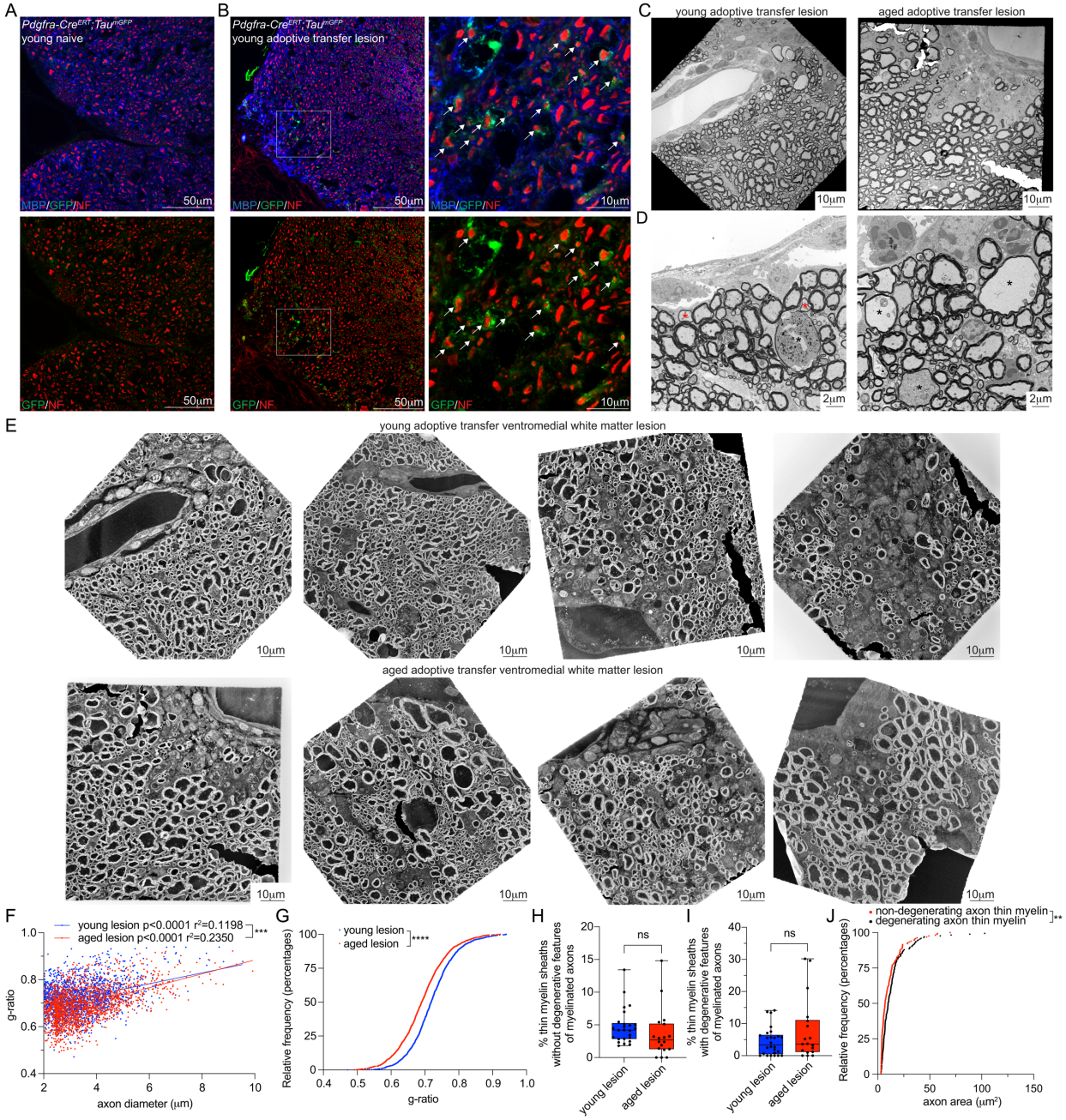

Figure 5- Remyelination in young and aged adoptive transfer lesions

(A). Representative image of lumbar ventrolateral spinal cord in lineage traced OPC Cre line crossed to membrane GFP reporter (*Pdgfra-Cre^{ERT};Tau^{mGFP}*) for labeling remyelinating myelin sheaths from OPCs. Staining for myelin (MBP), lineage traced OPC processes (GFP) and axons (NF) with no GFP+ myelin sheaths in naïve/non-adoptive transfer. **(B)**. Representative image of young *Pdgfra-Cre^{ERT};Tau^{mGFP}* ventral spinal cord 10 days post-adoptive transfer with lineage traced OPC GFP+ processes wrapping NF+ axons (arrows) at the lesion edge, box indicates region of higher magnification. (**C**). Representative transmission electron microscopy (TEM) images of ventromedial white matter lesions in young and aged adoptive transfer. (**D**). Higher magnification TEM images of a young adoptive transfer lesion with thin myelin sheaths around degenerating axons with electron dense material or myelin infoldings (black asterisks) and thin myelin sheaths around axons without signs of degeneration (red asterisks). (**E**). Representative TEM inverted images of young and aged adoptive transfer lesions to highlight myelin sheaths. (**F**). Quantification of g-ratios of axons ≥2µm diameter in young and aged adoptive transfer lesions. Simple linear regression analysis. (**G**). Cumulative relative frequency distribution of g-ratios indicating a significantly higher proportion of lower g-ratios (thicker myelin sheaths) in aged lesions. Kolmogorov-Shirnov test. (**H**). Quantification of percent of thin myelin sheaths (g-ratio ≥0.8) without degenerative features of total myelinated axons with diameter ≥2µm within a lesion. No significant difference between young and aged lesions. Median shift Bootstrap test. (**I**). Quantification of percent of thin myelin sheaths (g-ratio ≥0.8) with degenerative features of total myelinated axons with diameter ≥2µm within a lesion. No significant difference between young and aged lesions. Median shift Bootstrap test. (**J**). Cumulative relative frequency distribution of axonal areas of thin myelin sheaths with degenerative features (black) or no degenerative features (gray) with a significantly higher proportion of large axons in axons with degenerative features. Kolmogorov-Shirnov test. F-G, n=4 young animals with 31 lesions, n=6 aged animals with 36 lesions. H-J, n=4 young animals with 25 lesions, n=6 aged animals with 18 lesions. Box and whiskers plots: box 25 to 75 percentile, whiskers min to max, median line, show all datapoints. p value: ns, p>0.05, **p≤0.01, ***p≤0.001, ****p<0.0001.